PCH PhysicoChemical Hydrodynamics Vol. 10, No. 2, pp. 195–213, 1988.
Printed in Great Britain

0191–9059/88 $3.00+0.00
Pergamon Press plc

DOUBLE-DIFFUSIVE CONVECTION DURING DENDRITIC SOLIDIFICATION OF A BINARY MIXTURE

C. BECKERMANN* and R. VISKANTA

Heat Transfer Laboratory, School of Mechanical Engineering, Purdue University, West Lafayette, IN 47907, U.S.A.

(*Received* 4 *August* 1987)

Abstract—A combined experimental and numerical study is reported of dendritic solidification of an ammonium chloride–water solution inside a vertical rectangular enclosure. Based on the volumetric averaging technique, one set of conservation equations is derived, which is valid for the liquid and solid regions as well as for the dendritic mushy zone. Experiments are performed to visualize the phase-change and convection processes in the cavity. It is found that the solidification process induces a variety of double-diffusive phenomena in the liquid, including plumes and layering. These convection processes influence considerably the local solidification rates and can cause remelting in parts of the system. While it has been possible to qualitatively predict some of the phase-change and double-diffusive phenomena observed in the experiments, the numerical results show considerable disagreement with the measured data. The need for further analytical and experimental work on solidification of multicomponent mixtures is emphasized.

INTRODUCTION

Solid–liquid phase-change (solidification or melting) in multi-component systems occurs in many engineering, environmental, and technological processes, including solidification of castings and ingots, crystal growth, coating and purification of materials, welding, polymer production, freeze drying of food stuffs, latent heat energy storage, magmatic crystallization, freezing and melting in oceans, freezing of moist soil, etc. Phase-change in multi-component systems differs in many respects from solidification or melting of pure substances. Usually, the phase transformation takes place over a temperature range rather than at a discrete temperature. In other words, the solid and liquid phases can coexist at various temperatures, depending on the composition of the mixture. In addition, in most multi-component systems, a species has different solubilities in the liquid and solid phases. Hence, during phase-change a species may be preferentially incorporated or rejected at the solid–liquid interface. Furthermore, during solidification, the solid–liquid interface is not always smooth but a variety of microscopically complicated growth structures can develop (e.g. dendritic or faceted growth). The region characterized by the presence of such irregular interfaces is often called a mushy zone.

It is now well recognized that natural convection has a considerable influence on the phase-change processes in multi-component systems. Natural convection in the liquid phase is induced by both temperature and concentration gradients. Temperature gradients may be externally imposed (i.e. by heating–cooling of the system) and are generated internally by the release–absorption of the latent heat within the mushy zone. Concentration gradients are caused by the preferential incorporation or rejection of a species at the microscopic solid–liquid interfaces. Because most fluids have vastly different molecular diffusivities for

* Presently at the Department of Mechanical Engineering, The University of Iowa, Iowa City, Iowa 52242, U.S.A.

heat and species, a variety of double-diffusive convection patterns can develop in the liquid [1, 2]. The present study is concerned with the effects of double-diffusive natural convection on solidification in multi-component systems.

Experimental evidence of double-diffusive convection during solidification of multi-component mixtures has been obtained by researchers in the field of metallurgy, geophysics and oceanography [1, 2]. The importance of thermal and solutal natural convection during solidification of metallic alloys (Pb–Sn, Al–Cu, In–Sn) has been demonstrated more than two decades ago [3–6]. Because direct observation of the solidification and convection processes is not possible in metallic alloys, many researchers in the field of metallurgy have resorted to transparent model systems [7], such as alloys of various organic compounds (e.g. carbontetrabromide, succinonitrile, camphor, etc.) and aqueous solutions of a number of salts (e.g. NH_4Cl, Na_2CO_3, Na_2SO_4, K_2CO_3, etc.). Using such transparent alloys it has been possible to visualize the effects of double-diffusive convection on the grain structure [8] and chemical inhomogeneities (macrosegregation) [9–14] in solidifying castings. Interdendritic fluid flow (i.e. within the mushy zone) driven, in part, by thermal and solutal buoyancy forces, is now understood to be the major cause of a large variety of macrosegregation phenomena. For example, it has been shown that double-diffusive fingers are the cause of channel-type segregation ("freckles") in alloy castings [9–14]. Transparent model systems have also been utilized by geophysicists to study double-diffusive convection during magmatic crystallization [15–17]. Most of their work has concentrated on the formation of double-diffusive layers during solidification from the side. It has been found that the crystal growth rates can vary substantially within the double-diffusive layers. Double-diffusive effects during freezing of saline water from above and below have also been investigated [1, 15, 18, 19].

Despite the abundance of experimental evidence of double-diffusive phenomena during phase-change in multi-component systems, very little systematic work has been performed to quantitatively predict the transport processes in such systems. Modeling of dendritic solidification of binary alloys has been reported in the metallurgical literature [12, 13, 20–25]. In most models, however, the temperature or concentration distributions are assumed to be known in parts of the system or the convective flow between the pure liquid region and the mushy zone is not properly accounted for [12, 13, 20–25]. Not surprisingly, none of the previous studies have been able to predict any of the double-diffusive convection patterns observed in the experiments.

The objective of the present study is to develop a model through which the complicated convection and phase-change process during dendritic solidification of a binary mixture can be predicted. For this purpose, a simple physical system is selected consisting of a rectangular cavity with the vertical side walls held at uniform temperatures. Initially, the cavity is occupied by an ammonium chloride–water (NH_4Cl–H_2O) solution. NH_4Cl–H_2O solutions have been utilized in the past as model systems to study dendritic solidification [7–14]. The solution is solidified by lowering one of the vertical side walls below the liquidus temperature that corresponds to the initial concentration. A number of experiments are performed to visualize the convection and solidification phenomena in the present system as well as to verify the model predictions.

ANALYSIS

Mathematical formulation

During dendritic solidification of a binary mixture, three different regions can be identified. Beside the pure liquid and solid regions, a mushy zone exists consisting of a fine

meshwork of dendrites growing into the liquid region. It is in this mushy zone where the phase-change processes take place. In virtually all of the previous studies of dendritic solidification [12, 13, 20–24], the conservation equations have been derived separately for each region. The solution of such equations involves coupling of the three sets of equations by appropriate matching conditions between the regions. In the present study, an alternative approach is taken in order to avoid the difficulties associated with the solution of a multiple region problem.

The model equations are obtained by integrating the microscopic conservation equations over a small volume element. Such a volume element is simultaneously occupied by the liquid and solid phases of the binary mixture. While the microscopic conservation equations are only valid within each phase, the "averaged" equations account for the presence of the microscopic solid–liquid interfaces and are valid over the entire volume element. As mentioned previously, microscopically complicated interfacial structures are characteristic of the mushy zone which is formed during (dendritic) solidification of binary mixtures. Since the volumetric averaging is performed for arbitrary fractions of the liquid and solid phases within the volume element, the averaged equations are, however, not only valid in the mushy zone but also in the pure liquid and solid regions. Hence, the present approach offers the advantage that the entire system can be treated as a single domain governed by one set of conservation equations. Although it may be possible to obtain similar model equations directly from macroscopic balance considerations, it is believed that a rigorous averaging process will offer additional insight into the assumptions involved [40].

In the derivation of the volume averaged equations the following simplifying assumptions are made:

1. The transport processes are two-dimensional and laminar.
2. The properties of the solid and liquid phases are homogeneous and isotropic.
3. The solid and liquid in the mushy zone are in local thermal and phase equilibrium.
4. The solid is stationary and rigid.
5. The Boussinesq approximation can be invoked.
6. The thermophysical properties are constant, but may be different for the liquid (l) and solid (s) phases.
7. Dispersion fluxes due to velocity fluctuations are negligibly small.
8. Velocities due to density change upon phase-change are neglected.

The averaging process of the microscopic conservation equations for each phase is described in detail elsewhere [26–29] and does not need to be repeated here. It should be mentioned, however, that the mass, energy, and species equations are obtained by combining the averaged conservation equations for the solid and liquid phases, while the momentum equation represents the averaged equation for the liquid phase only. The averaged equations, valid in the liquid and solid regions as well as the mushy zone, can be summarized as [29]:

Continuity:

$$\nabla \cdot \mathbf{U} = 0 \tag{1}$$

Momentum:

$$\frac{\rho_l}{\varepsilon}\frac{\partial \mathbf{U}}{\partial t} + \frac{\rho_l}{\varepsilon^2}(\mathbf{U}\cdot\nabla)\mathbf{U} = -\nabla P + \frac{\mu_{l,\mathrm{eff}}}{\varepsilon}\nabla^2\mathbf{U} - \left(\frac{\mu_l}{K} + \frac{\rho_l F}{K^{1/2}}|\mathbf{U}|\right)\mathbf{U} - \rho_l \mathbf{g}[\beta_T(T_l - T_{\mathrm{ref}}) + \beta_C(C_l - C_{\mathrm{ref}})] \tag{2}$$

Energy:

$$\frac{\partial}{\partial t}[\varepsilon\rho_l h_l + (1-\varepsilon)\rho_s h_s] + \nabla\cdot(\rho_l h_l \mathbf{U}) = \nabla\cdot[\varepsilon k_{l,\text{eff}}\nabla T_l + (1-\varepsilon)k_{s,\text{eff}}\nabla T_s] \tag{3}$$

Species:

$$\frac{\partial}{\partial t}[\varepsilon\rho_l C_l + (1-\varepsilon)\rho_s C_s] + \nabla\cdot(\rho_l C_l \mathbf{U}) = \nabla\cdot[\varepsilon\rho_l D_{l,\text{eff}}\nabla C_l + (1-\varepsilon)\rho_s D_{s,\text{eff}}\nabla C_s]. \tag{4}$$

In the above equations, $\mathbf{U}$ represents a superficial velocity and is defined as

$$\mathbf{U} = \varepsilon\mathbf{U}_l \tag{5}$$

where $\mathbf{U}_l$ and ε are the average velocity of the liquid and the volume fraction liquid, respectively.

The third and fourth terms on the RHS of equation (2) are empirical expressions to account for first and second order drag forces, respectively, between the liquid and the rigid solid phase. The permeability, K, is a function of the liquid fraction, ε, and the structure of the dendritic mushy zone. In analogy with flow in porous media, K is calculated in the present study utilizing the Kozeny–Carman equation

$$K = \frac{\varepsilon^3}{5M_s^2(1-\varepsilon)^2} \tag{6}$$

where M_s is the volumetric specific surface area of a typical dendrite arm. Assuming the shape of a dendrite arm to be a slender cone of base diameter d, M_s can be approximated as [12]

$$M_s \approx 6/d \tag{7}$$

where d is of the order of 10^{-4} m [12]. Similarly, the inertia coefficient, F, can be calculated from [30] to be

$$F = 0.13\varepsilon^{-3/2}. \tag{8}$$

Note that by neglecting the inertia and viscous terms in equation (2), the momentum equation reduces to the familiar Darcy law [26], which has frequently been utilized to model the flow in a dendritic mushy zone [12, 13, 20–24]. On the other hand, in the pure liquid region ($\varepsilon \to 1$), equation (2) reduces to the usual "Boussinesq" equation for a pure liquid. In the solid region ($\varepsilon \to 0$), the permeability and, thus, the velocities approach zero. Hence, by using the local value of the liquid fraction, ε, in the solution of the momentum equation, the flow is correctly calculated in all regions of the domain.

The quantities μ_{eff}, k_{eff} and D_{eff} in equations (2)–(4) represent effective "diffusion" coefficients, which also account for the presence of the other phase in the volume element. Exact expressions for these quantities can be found in the literature [26–28]. Some terms in these expressions are, however, difficult to evaluate, because of the complicated interfacial structures in the mushy zone. As a first approximation, the effective properties of each phase are taken equal to their respective values in the absence of the other phase.

In writing the energy conservation equation, equation (3), the assumption of local thermal equilibrium between the liquid and solid phases has not yet been utilized (see assumption 3). Local thermal equilibrium implies that the liquid and solid phases within the volume element used for the averaging process have the same temperature, i.e. $T_l = T_s = T$. In addition, the difference between the liquid and solid enthalpies in the mushy zone (i.e. for $0 < \varepsilon < 1$) is exactly equal to the latent heat, Δh. Expanding the first term on the RHS of equation (3) utilizing the above assumption results, after a few steps [29], in

$$\overline{\rho c}\frac{\partial T}{\partial t}+\rho_l c_l \mathbf{U}\cdot\nabla T=\nabla\cdot(\bar{k}\nabla T)-\rho_l\Delta h\frac{\partial \varepsilon}{\partial t} \tag{9}$$

where the mean thermal capacitance, $\overline{\rho c}$, and thermal conductivity, $\bar{k}$, of the solid–liquid mixture are defined as

$$\overline{\rho c}=\varepsilon\rho_l c_l+(1-\varepsilon)\rho_s c_s \tag{10}$$

$$\bar{k}=\varepsilon k_l+(1-\varepsilon)k_s. \tag{11}$$

The last term on the RHS of equation (9) accounts for the (volumetric) latent heat release in the mushy zone. This term is equal to zero in regions where no phase-change takes place (i.e. $\varepsilon=$ const.). Equation (9) reduces to the correct limits for $\varepsilon\to 0$ or 1 (i.e. the pure solid and liquid regions) and can, thus, be utilized throughout the entire domain.

Neglecting diffusion of species in the solid phase, the species conservation equation, equation (4), can be rewritten as

$$\frac{\partial}{\partial t}(\bar{\rho}C)+\rho_l\mathbf{U}\cdot\nabla C_l=\rho_l\nabla\cdot(\varepsilon D_l\nabla C_l) \tag{12}$$

where the mean density, $\bar{\rho}$, and average concentration, C, of the solid–liquid mixture are defined as

$$\bar{\rho}=\varepsilon\rho_l+(1-\varepsilon)\rho_s \tag{13}$$

$$C=(\varepsilon\rho_l C_l+(1-\varepsilon)\rho_s C_s)/\bar{\rho}. \tag{14}$$

Again, equation (12) reduces to the correct limits for $\varepsilon\to 0$ or 1, and can, thus, be utilized in the mushy zone as well as in the pure liquid and solid regions.

With the assumption of local phase equilibrium, the concentrations of the solid and liquid phases (C_s and C_l, respectively) in the volume elements within the mushy zone (i.e. for $0<\varepsilon<1$) are related to the temperature ($T=T_l=T_s$) through the equilibrium phase diagram of a particular binary mixture. For the aqueous solution considered in the present study (see Experiments) the solidus and liquidus curves are well approximated by the linear relationships

$$C_l=(T-T_p)/\Gamma \quad \text{for } 0<\varepsilon<1 \tag{15}$$

$$C_s=\kappa C_l \quad \text{for } 0<\varepsilon<1. \tag{16}$$

With the knowledge of T and C from the solution of equations (9) and (12) [and, of course, equations (1) and (2)], the local liquid fraction, ε, can be calculated from the phase diagram relationships and the definition of C. Combining equations (14)–(16) and solving for ε yields

$$\varepsilon(T,C)=\frac{\bar{\rho}C-\rho_s\kappa(T-T_p)/\Gamma}{(\rho_l-\rho_s\kappa)\,(T-T_p)/\Gamma}. \tag{17}$$

Equation (17) is nothing else but a modified form of the so-called "lever rule".

DIMENSIONLESS EQUATIONS

In order to illustrate the utility of the present model for dendritic solidification of a binary mixture, a sample problem is now selected and the relevant dimensionless parameters are identified. The physical system considered in the present study is shown in Fig. 1. The

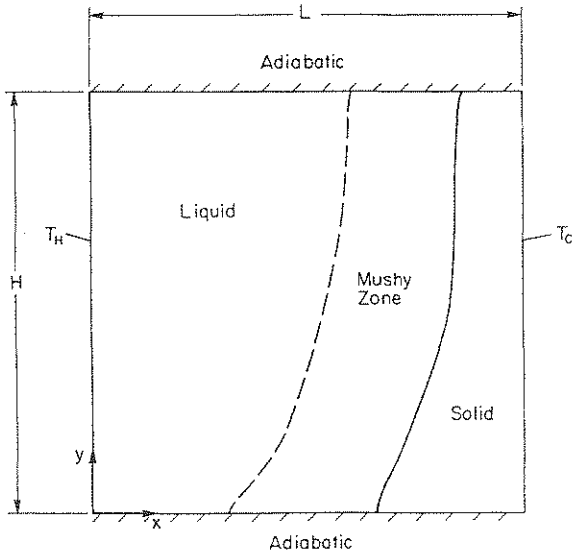

Fig. 1. Schematic of the physical model and coordinate system.

vertical walls of the rectangular enclosure are of height H and are held at the temperatures T_H and T_C. The connecting horizontal walls of length L are considered adiabatic. The enclosure is filled with a binary fluid of concentration C_{in}. Initially, the system is at a uniform temperature, T_{in}, equal to T_H, where T_H is above the liquidus temperature corresponding to the initial concentration, C_{in}. The solidification process is initiated by lowering the temperature of the right vertical sidewall to T_C, where T_C is below the liquidus temperature.

The dimensionless parameters governing this system are obtained by introducing dimensionless variables (see Nomenclature) into the model equations. The resulting dimensionless equations are

$$\nabla \cdot \mathbf{u} = 0 \tag{18}$$

$$\frac{1}{\varepsilon}\frac{\partial \mathbf{u}}{\partial \tau} + \frac{1}{\varepsilon^2}(\mathbf{u}\cdot\nabla)\mathbf{u} = -\nabla p + \frac{Pr}{\varepsilon}\nabla^2\mathbf{u} - \left[\frac{Pr}{Da} + \frac{F}{Da^{1/2}}|\mathbf{u}|\right]\mathbf{u} + Ra\,Pr\,(\Theta + R_s\Phi)\mathbf{e}_y \tag{19}$$

$$(\rho c)^* \frac{\partial \Theta}{\partial \tau} + \mathbf{u}\cdot\nabla\Theta = \nabla\cdot(k^*\nabla\Theta) - \frac{1}{Ste}\frac{\partial \varepsilon}{\partial \tau} \tag{20}$$

$$\frac{\partial}{\partial \tau}(\rho^*\Phi) + \mathbf{u}\cdot\nabla\Phi_l = \nabla\cdot\left(\frac{\varepsilon}{Le}\nabla\Phi_l\right). \tag{21}$$

In addition, the phase diagram relationships can be written in dimensionless form as

$$\Phi_l = (\Theta - \Theta_p)/\gamma \quad \text{for } 0 < \varepsilon < 1 \tag{22}$$

$$\Phi_s = \kappa\Phi_l \quad \text{for } 0 < \varepsilon < 1 \tag{23}$$

while the equation for the liquid fraction, equation (17), becomes

$$\varepsilon(\Theta, \Phi) = \frac{\rho^*\Phi - \rho_s^*\kappa(\Theta - \Theta_p)/\gamma}{(1 - \rho_s^*\kappa)(\Theta - \Theta_p)/\gamma}. \tag{24}$$

The dimensionless boundary and initial conditions for the physical system considered in the present study are

$$\mathbf{u} = 0, \quad \Theta = 1, \quad \frac{\partial \Phi}{\partial \xi} = 0 \quad \text{at} \quad \zeta = 0, \quad 0 \leqslant \eta \leqslant A$$

$$\mathbf{u} = 0, \quad \Theta = 0, \quad \frac{\partial \Phi}{\partial \xi} = 0 \quad \text{at} \quad \zeta = 1, \quad 0 \leqslant \eta \leqslant A \tag{25}$$

$$\mathbf{u} = 0, \quad \frac{\partial \Theta}{\partial \eta} = 0, \quad \frac{\partial \Phi}{\partial \eta} = 0 \quad \text{at} \quad \eta = 0, A, \quad 0 \leqslant \xi \leqslant 1$$

$$\mathbf{u} = 0, \quad \Theta = 1, \quad \Phi = \Phi_{in} \quad \text{for} \quad \tau \leqslant 0. \tag{26}$$

Solution procedure

The dimensionless conservation equations, equations (18)–(21), were solved numerically utilizing the iterative SIMPLER algorithm [31]. The algorithm is based on a fully-implicit discretization scheme for the unsteady terms, while the power-law scheme is utilized to approximate the combined convective and diffusive fluxes. The last three terms on the RHS of equation (19) as well as the latent heat term in equation (15) represent source terms and are treated according to the procedure outlined in the literature [31].

As discussed previously, the governing equations are valid in the pure liquid and solid regions as well as in the mushy zone. Consequently, there is no need to track explicitly the geometrical shape and extent of each region. Hence, a fixed and regular grid system can be utilized in the numerical solution scheme and one set of equations is solved on this grid throughout the physical domain. A special procedure is required for the solution of the species conservation equation, equation (21), in the mushy zone, because of the simultaneous presence of Φ and Φ_l. This procedure as well as other details of the numerical algorithm are given elsewhere [29].

In the calculations reported in the present study, a grid of 50×50 nodal points was utilized. The grid was slightly skewed in the $\xi-$ and η-directions to provide a higher concentration of nodal points near the walls of the enclosure where velocity, thermal, and concentration gradients need to be accurately resolved. It is realized that this grid system might not be adequate to resolve all details of the double-diffusive flow structures in the liquid region. The selected mesh size should only be viewed as a compromise between accuracy and computational cost. Additional tests of the accuracy of the numerical algorithm were performed for the limiting cases of phase-change in a fully porous medium [32] and natural convection in fully fluid and fully porous enclosures [33], and good agreement was found between predictions and results reported in the literature.

A dimensionless time step of $\Delta\tau = 5.9 \times 10^{-5}$ ($\Delta t = 1$ s) was utilized in the numerical simulations to assure small changes in the liquid fraction at each time step. For each time step, the iterations were terminated when the dependent variables agreed to four significant figures at each nodal point and the residual source of mass was less than 1×10^{-5}. In addition, convergence was checked by performing overall energy and species balances. For a total simulation time of approximately $\tau = 0.216$ ($t = 1$ h), the calculations required more than 10 000 CPU seconds on a CYBER 205 digital computer.

EXPERIMENTS

Experiments were performed in a well insulated test cell of square cross-section [29]. The test cell had inside dimensions of 4.76 cm in height and width and 3.81 cm in depth. The horizontal bottom wall was constructed of a phenolic plate, while the top wall and the

Table 1. Summary of experimental test conditions

T_H(K)	T_C(K)	C_{in}	A	Pr	Le	Ra	R_s	Ste
307.5	273.15	0.7	1.0	9.03	74.25	8.639×10^7	15.67	0.3557

Θ_p	γ	κ	$\rho^*(\varepsilon = 0)$	$k^*(\varepsilon = 0)$	$(\rho c)^*(\varepsilon = 0)$
10.459	−10.917	0.3	1.023	0.840	0.589

vertical front and back walls were made of Lexan.® The two vertical side walls, which served as the heat source/sink, were multipass heat exchangers machined out of a copper plate. The heat exchangers were connected through a valve system to two constant temperature baths (Haake A82). The temperatures of each heat exchanger were measured and found to be uniform to within 0.1°C of the desired temperature. Measurement of the temperature distribution inside the test cell was made with 33 thermocouples that were placed in three different rakes such that the temperatures were measured along the vertical centerplane of the test cell. All thermocouples were calibrated with an accuracy of ±0.1°C.

Qualitative observations of the density distribution and the flow structure in the liquid region were made using a shadowgraph system. The light source consisted of a collimated beam from a mercury-arc lamp. After passing through the test cell, the light was imaged on a white glass plate and photographed using a high-sensitivity film (Kodak Tmax 400). Concentration measurements were performed by withdrawing a few drops of the liquid with a hypodermic needle at the desired location in the test cell and analyzing them with a refractometer (Kernco). The refractometer was calibrated for the aqueous solution used in the present experiments (i.e. NH_4Cl–H_2O) with an accuracy of ±0.2 wt% (NH_4Cl). Finally, it should be mentioned that the various measurements (see above) were conducted in separate tests so that they did not interfere with each other.

In the solidification experiments, a solution of ammonium chloride (NH_4Cl) in water (H_2O) was utilized as the binary phase-change material. During solidification of NH_4Cl–H_2O solutions, dendritic crystals are formed [9–14]. The equilibrium phase diagram of the NH_4Cl–H_2O system is of the eutectic type with a eutectic temperature, T_E, and concentration, C_E, of 257.75K and 0.803 weight fraction H_2O, respectively [9–14, 34]. A number of experiments with different initial and boundary conditions were performed [29]. As a representative example and for comparison purposes with the numerical simulation, only one of these experiments is presented in this paper. The experimental conditions together with the values of the dimensionless parameters for this experiment are summarized in Table 1. All properties were evaluated at the mean temperatures and concentrations [9–14, 34].

RESULTS AND DISCUSSION

Experimental results

The time evolution of the solidification process can be seen from the shadowgraph images, Figs 2–4. When the NH_4Cl–H_2O solution starts to solidify, solid dendrites are formed at the right vertical wall. Initially (see Fig. 2a), some of these dendrites are not firmly attached to the heat exchanger, descend downwards along the right wall, and form a layer of dendrite debris at the bottom. After approximately 3 min into the experiment, no more dendrites are observed to float in the liquid (see Fig. 2b) and solidification proceeds mainly from the

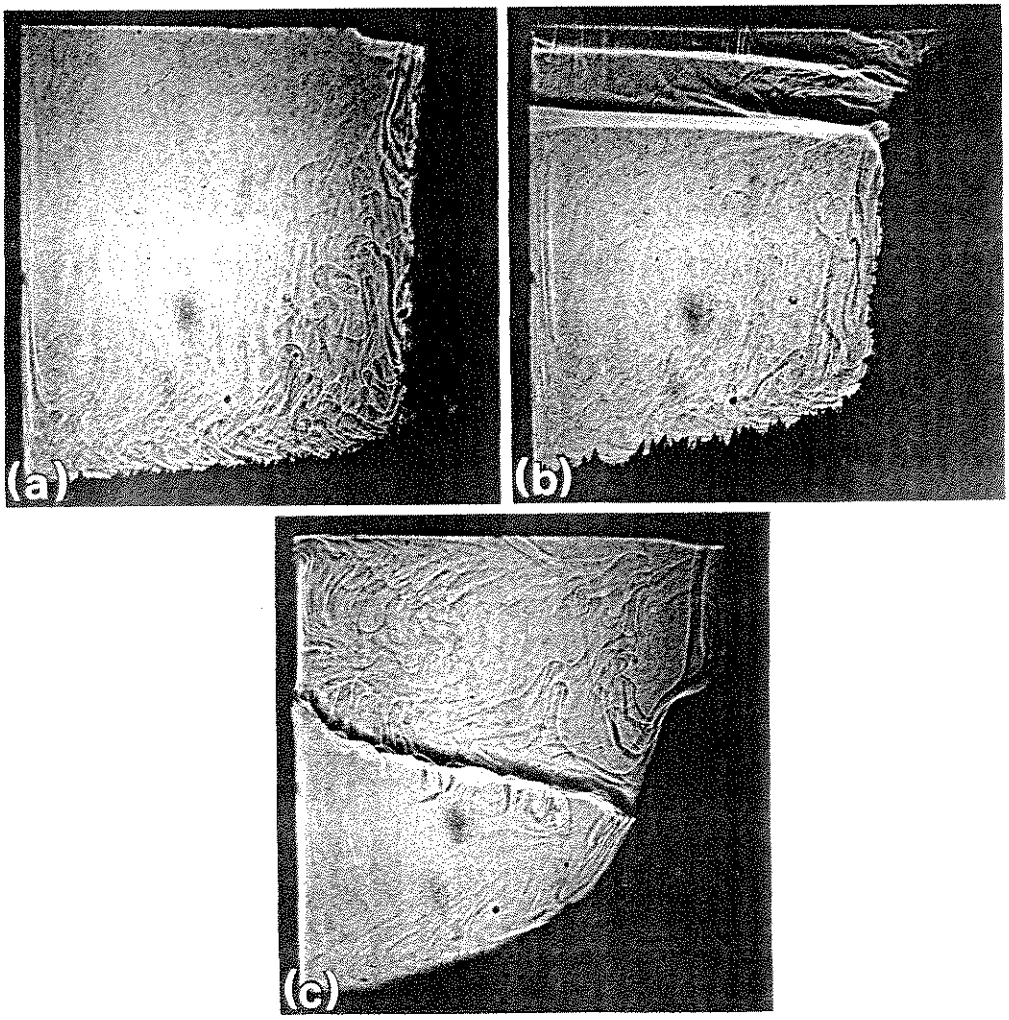

Fig. 2. Shadowgraphs showing the development of the double-diffusive layers. (a) $t = 3$ min; (b) $t = 15$ min; (c) $t = 100$ min.

cold (right) wall. Note that for the conditions of the present experiment no pure solid region ($\varepsilon = 0$) exists in the test cell, because the cold wall is above the eutectic temperature (see Table 1).

According to the equilibrium phase diagram of the NH_4Cl–H_2O system, the solid dendrites have a higher NH_4Cl concentration than the remaining liquid. In other words, H_2O is partially rejected at the microscopic solid–liquid interfaces resulting in an increase in the H_2O concentration and, hence, a decrease in the density of the liquid in the mushy zone. The water-rich liquid effectively retains its composition because of its low mass diffusivity. As can be seen from Fig. 2, some of this liquid leaves the mushy zone horizontally and rises up in plumes, through the liquid of the original composition, to the top of the cavity. Another portion of the water-rich liquid formed during the solidification process flows directly upwards and leaves the mushy zone in the uppermost region of the test cell. There, it spreads horizontally and accumulates in a layer of water-rich liquid above the liquid of the original composition. The formation of this layer can clearly be seen from the shadowgraph

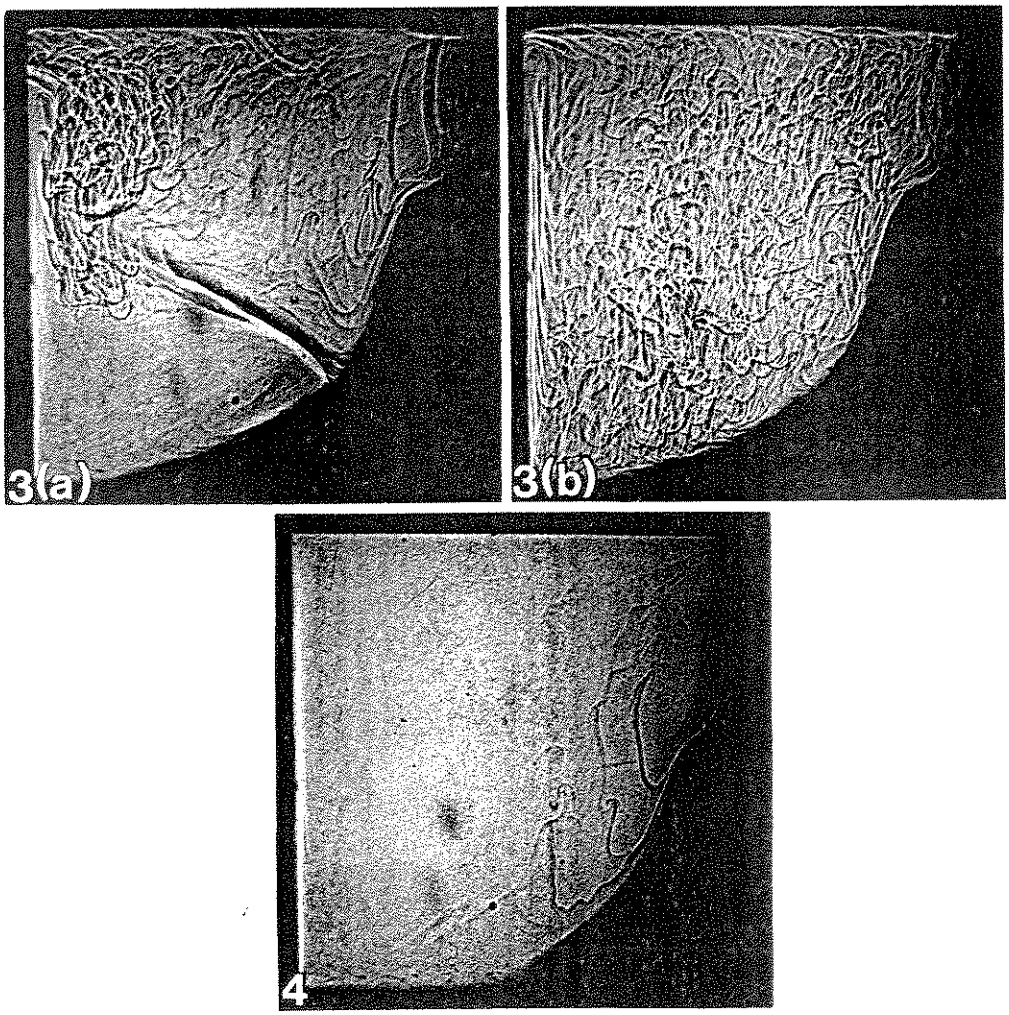

Fig. 3. Shadowgraph showing the break-up and mixing of the double-diffusive layers. (a) $t = 103$ min; (b) $t = 106$ min.

Fig. 4. Shadowgraph showing the approach to steady-state ($t = 240$ min).

images, Fig. 2. The top layer is separated by a sharp ("double-diffusive") interface from the liquid in the lower portion of the test cell. As solidification progresses, the vertical extent of the top layer continues to increase at the expense of the liquid in the lower layer. At $t = 15$ min (Fig. 2b), a second interface starts to appear above the original one. This second interface is, however, not stable and recedes back toward the mushy zone [29].

The results of additional flow visualization experiments reported in [29] indicate that a clockwise rotating recirculation cell exists within the bottom layer. This convection cell is caused by thermal buoyancy forces. The liquid in the bottom layer is heated by the hot (left) wall and rises up. Since the mass diffusivity is much lower than the thermal diffusivity ($Le \gg 1$), it retains its original composition and can only rise until it reaches a level where the density decrease due to the heating is equal to the density decrease caused by the presence of the water-rich liquid in the upper portion of the test cell. At that level, the flow

turns horizontal towards the mushy zone where it is cooled again. Eventually, a clockwise rotating convection cell is established in the lower layer. Since the flow is constrained by the water-rich liquid at the top of the cavity, a definite interface is formed above the convection cell. The development of such distinct ("double-diffusive") interfaces in a compositionally stratified fluid is well known for sidewall cooling/heating and has been studied in other contexts [35]. As can be seen from Fig. 2(c), the thermal buoyancy forces cause a similar convection cell in the water-rich top layer. This is, however, only evident at later times when the top layer reaches a certain thickness.

The water-rich plumes originating in the mushy zone are somewhat affected by the thermal natural convection flow in the liquid region (see Figs 2a–c). Because of the relatively strong flow downwards along the mushy zone, the plumes describe a curved path. This phenomenon reflects the opposing sense of the thermal and solutal buoyancy forces in the liquid in and adjacent to the mushy zone. For the present conditions, however, the solutal buoyancy forces are much stronger than the ones due to thermal effects ($R_s \approx 15.7$), so that the plumes as well as the liquid in the mushy zone flow mostly upwards.

The double-diffusive convection patterns in the liquid have a profound influence on the solidification process itself (see Figs 2a–c). In the region below the water-rich top layer, the shape of the mushy zone is predominantly influenced by the thermal natural convection flow. During the initial 30 min (Figs 2a and b), dendrites grow from the vertical, cold wall and, to a lesser extent, from the adiabatic bottom wall of the cavity. Solidification takes place at the bottom because the temperature of the liquid decreases as it flows downwards along the mushy zone. After some time, the horizontal extent of the mushy zone increases smoothly towards the bottom of the enclosure (see Fig. 2c). Also note that in the later stages of the experiment, the tips of the dendrites growing into the liquid region as well as the dendrites at the bottom, close to the left (hot) wall, are remelted, resulting in a "smoother" appearance of the mushy zone. This remelting is even more pronounced in the top layer. The higher water concentration in the top layer results in a lower liquidus temperature causing a complete termination of the solidification process in the upper region of the test cell. Since the vertical extent of the top layer increases with time, an increasing portion of the mushy zone is surrounded by the water-rich liquid. Consequently, some of the dendrites in this region remelt and the horizontal extent of the mushy zone becomes smaller. This relatively strong dependence of the solidification process on the concentration of the liquid is reflected by the "step" change in the horizontal extent of the mushy zone at the vertical location where the double-diffusive interface is present (see Figs 2b and c).

Interestingly, after approximately 90 min the double-diffusive interface, separating the two liquid layers of different concentration, becomes increasingly tilted downwards away from the left wall. At $t = 100$ min (Fig. 2c), the interface has a wavy appearance, while its tilt is more than 20° from the horizontal. Then, within the next 6 min (see Figs 3a and b), the interface breaks up and violent mixing occurs between the liquid in the upper and lower layers. At $t = 106$ min (Fig. 3b) the entire liquid region is affected by this mixing process. The instability and break up of the interface described above is due to several reasons. Due to the remelting, the water concentration in the upper layer decreases with progressing time (see Fig. 7). On the other hand, the water concentration in the lower layer continues to increase, because in this region solidification takes place, while the plumes originating in the mushy zone carry water-rich liquid into the lower layer. As a result the concentrations in the upper and lower layer become increasingly equal. With a relatively small concentration difference across the double-diffusive interface, the thermal buoyancy forces become dominant over the solutal ones. Since the thermal natural convection flow is upward at the left (hot) wall, the interface adjacent to this wall is "pressed" towards the top of the enclosure. The opposite is true for the interface adjacent to the mushy zone. This explains the strong

tilt of the double-diffusive interface before the break-up occurs. Eventually, the thermal natural convection flow penetrates the double-diffusive interface resulting in the mixing of the fluid in the two layers.

After the mixing of the liquid in the two layers is completed (Fig. 4), the concentration in the liquid is relatively uniform (see Fig. 7). The flow in the liquid region is now characterized by a single clockwise rotating convection cell, with a few water-rich plumes ascending from the mushy zone towards the top. As can be seen from Fig. 4, some additional remelting occurs during the later stages of the experiment. This is particularly evident in the (lower) portion of the cavity where the mushy zone was previously bounded by the liquid of the lower layer. The system reaches a steady state shortly after $t = 240$ min.

Numerical predictions and comparison with the experiment

Due to space limitations, only a few representative results of the numerical simulation of the experiment are presented here. A complete record and discussion of the numerical results can be found elsewhere [29]. Predicted streamlines, isotherms and concentration isoplets are shown for $t = 5$ min ($\tau = 1.770 \times 10^{-2}$) and 60 min ($2.831 \times 10^{-1}$) in Figs 5 and 6, respectively. The dashed line in these figures indicates the boundary between the mushy zone and the pure liquid region (i.e. where $\varepsilon = 0.999$).

The predicted results for $t = 5$ min (Figs 5a–c) show that the mushy zone has reached a thickness of approximately 20% of the total length of the enclosure. At the top of the cavity, however, the extent of the mushy zone is very small, while there is some additional growth at the bottom wall. The flow inside the mushy zone is very weak (see Fig. 5a), indicating that the permeability of the dendritic structure is relatively small. Accordingly, the isotherms (Fig. 5b) are almost vertical and equally spaced and heat transfer is mostly by conduction. This relatively weak flow in the mushy zone, however, advects liquid of a higher H_2O content and a lower temperature upwards toward the top of the enclosure, where it leaves the mushy zone and spreads horizontally. The formation of a cold and water-rich top layer can clearly be seen from the predicted isoplets of the liquid concentration, Fig. 5(c). Besides the spreading of the liquid arriving from the mushy zone, the flow in this top layer is relatively weak. On the other hand, the liquid below the top layer is of a uniform concentration, equal to Φ_{in}. As shown in Fig. 5a, there exists a clockwise rotating convection cell in this bottom layer that is caused by thermal buoyancy forces. The predicted streamlines also show that the convection cell is effectively confined by the mushy zone and the top layer, so that there is almost no flow between the bottom layer and the other regions of the enclosure.

The two convection cells are predicted to merge several times between $t = 5$ and 60 min [29]. The predicted merging processes are due to the same reasons as described in the previous section. The intermediate results also indicate the presence of complicated flow patterns and recirculation cells in the core of the convection cell in the bottom layer [29]. Due to excessive computer time requirements, the numerical simulation was terminated at $t = 60$ min. The predicted results for $t = 60$ min are shown in Figs 6 (a–c). It can be seen that the mushy zone adjacent to the bottom layer is considerably larger than at earlier times, while its horizontal extent increases smoothly towards the bottom of the enclosure. On the other hand, the horizontal extent of the mushy zone next to the water-rich top layer continues to be very small. At the very top of the enclosure, the formation of a third layer can be observed (see Figs 6a and c), where the water-rich liquid originating in the mushy zone accumulates. Again, very little flow is predicted to occur between the liquid in the lower two layers and the mushy zone.

A comparison between the numerical results and the shadowgraph images (Figs 2–4) reveals that the predicted phase-change and double-diffusive layering processes are in

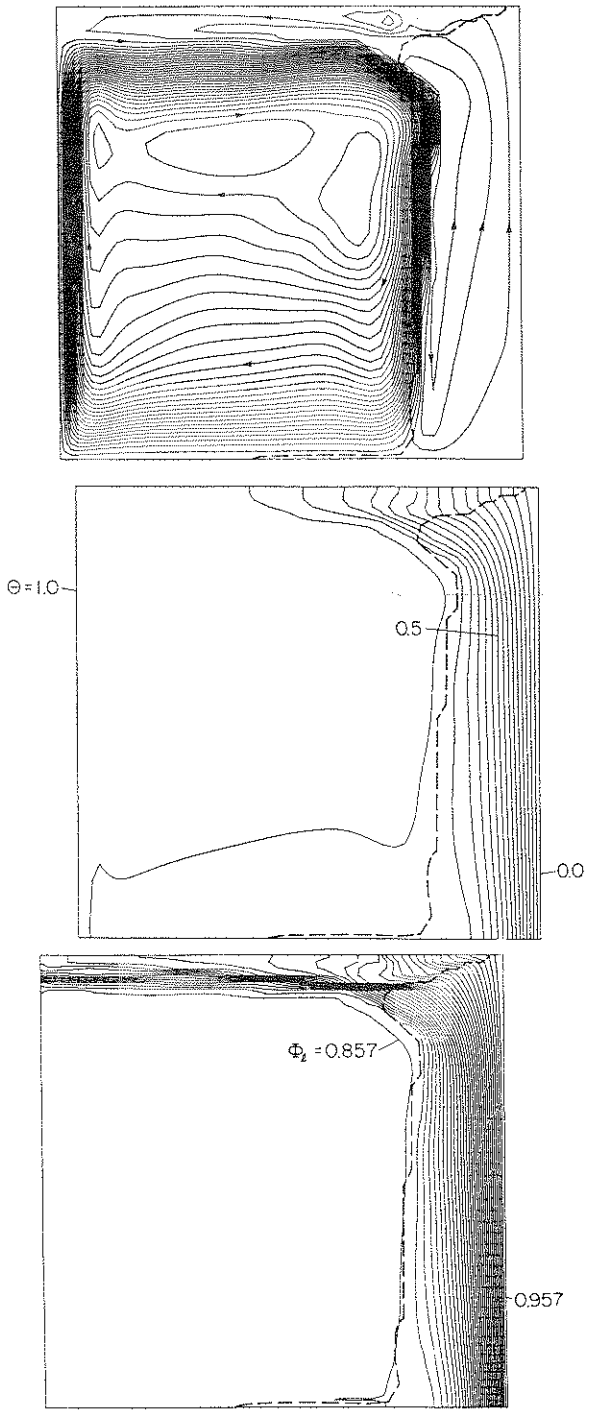

Fig. 5. Predicted results at $t = 5$ min. (a) Streamlines ($\psi_{min} = -44.48$, $\psi_{max} = 5.39$, equal increments). (b) Isotherms (equal increments). (c) Isoplets of liquid concentration (equal increments).

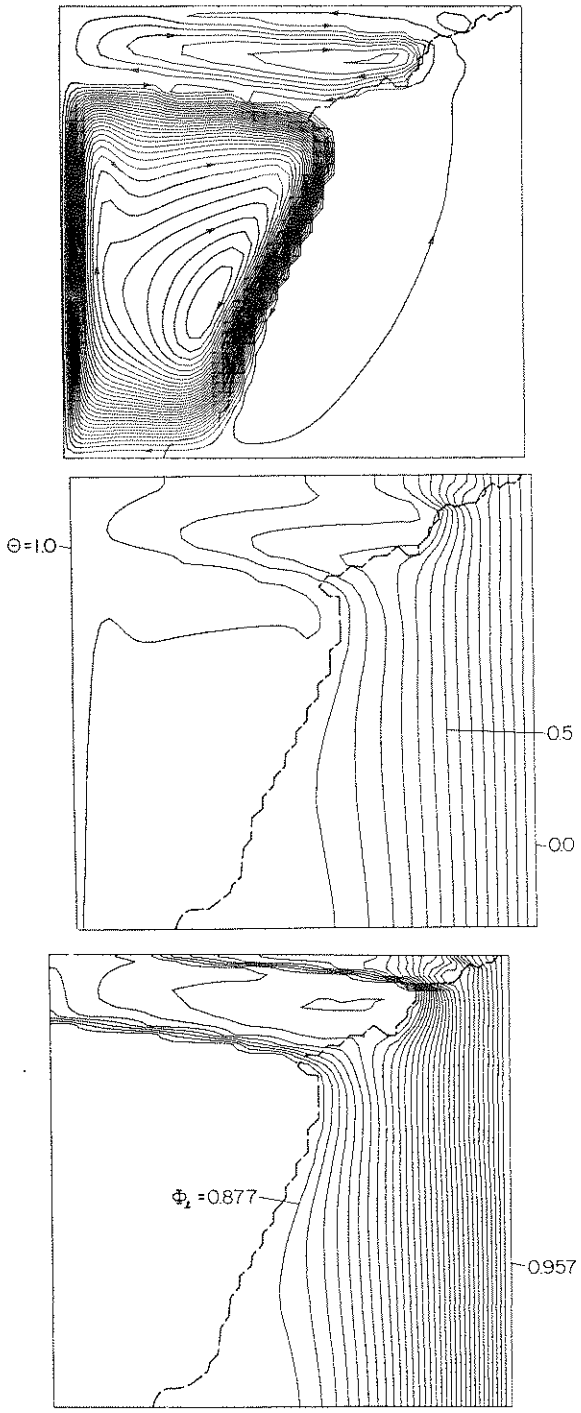

Fig. 6. Predicted results at $t = 60$ min. (a) Streamlines ($\psi_{min} = -60.80$, $\psi_{max} = 2.71$, equal increments). (b) Isotherms (equal increments). (c) Isoplets of liquid concentration (equal increments).

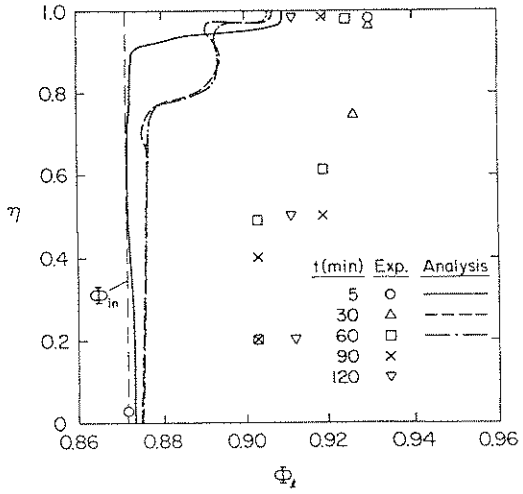

Fig. 7. Comparison of measured and predicted concentrations at $\xi = 0.5$.

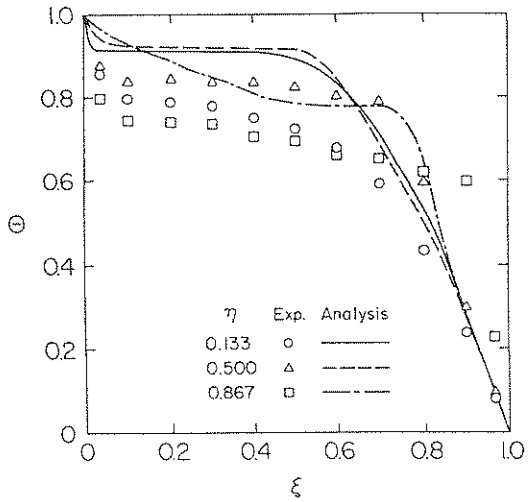

Fig. 8. Comparison of measured and predicted temperatures at $t = 60$ min.

qualitative agreement with the experimental results. There are, however, significant differences in the growth rates of the mushy zone and the double-diffusive layers as well as in the merging processes of the layers. These differences are further delineated by quantitative comparisons of the measured and predicted concentrations and temperatures, which are shown in Figs 7 and 8, respectively. It can be seen from Fig. 7 that during the initial 60 min, the measured concentrations of the liquid at the top of the cavity ($\eta = 0.98$, $\xi = 0.5$) are significantly higher than the predicted ones. The same is true for the liquid in the bottom layer (e.g. at $t = 60$ min). The measured and predicted temperatures, shown in Fig. 8 are in good qualitative agreement, while the absolute values differ by as much as 15% of the total temperature difference across the test cell.

The above differences between the measured and predicted results may be due to several reasons. First, there is a considerable uncertainty associated with the calculation of the "structural" parameters of the dendritic mushy zone, such as the permeability. Furthermore, the mushy zone (i.e. the dendrites) is in reality, highly anisotropic, which is not modeled in the present study. Relatively small differences in the structural parameters, however, are

expected to exert a significant influence on the fluid flow in the mushy zone. Since this flow is responsible for the formation and growth of the double-diffusive layers, the predicted results in all regions of the domain are strongly dependent on the calculation of the structural parameters. Additional experimental and analytical work is required for proper modeling of the structure of the mushy zone. It should be noted, however, that such modifications can easily be accommodated in the present model. Second, the shadowgraph images (Figs. 2a–c) show the existence of plumes, which originate at various locations inside the mushy zone and carry water-rich liquid into the pure liquid region. As indicated by the concentration measurements, these plumes mix with the liquid in both the upper and lower layers causing the (H_2O) concentrations in the layers to increase. The numerical simulation, however, does not predict a significant exchange of fluid between the lower layer and the mushy zone (see above) so that the concentration in the lower layer stays very close to the initial concentration (see Fig. 8). In view of the highly three-dimensional and transient nature of the plumes, this is not surprising and it is not clear at the present time how these complicated flow structures can be appropriately modeled. Third, a major problem in the present model is associated with the break-up and merging processes of the double-diffusive layers. As can be seen from the shadowgraph images (e.g. Figs 3a and b), the instabilities of the double-diffusive interface as well as the mixing of the liquid in the two layers can be characterized as highly chaotic. Considering the complicated structures and shapes of the mushy zone and the liquid region as well as the highly transient nature of the double-diffusive processes, a significant amount of additional research is required for the development of a model for such chaotic, double-diffusive flows. Fourth, some discrepancies between the measured and predicted results may be attributed to the floating and settling of crystals in the liquid region observed during the initial stages of the experiment. Obviously, the case of a non-stationary solid phase is not included in the present model. Although it is possible to derive the proper momentum equations for such a case, it is not clear how the detachment process of the crystals from the stationary dendritic structure can be modeled realistically. Fifth, the grid system utilized in the present numerical simulation cannot be considered adequate for resolving the double-diffusive interfaces present in the liquid region (see Figs 5c and 6c). In view of the high computational costs, new techniques must be developed to deal with the strong gradients associated with a double-diffusive interface. A moving grid system with a high concentration of nodal points in regions characterized by strong gradients might be useful in this respect. Finally, some differences between the measured and predicted temperatures and concentrations may be due to problems in the experimental set-up, including imperfect adiabatic and constant temperature boundary conditions, as well as uncertainties in the thermocouple and refractometer locations or readings. In addition, uncertainties and variations in the thermophysical and effective properties and inaccuracies associated with the numerical algorithm may be the cause of some deficiencies in the numerical simulation.

CONCLUSIONS

A combined experimental and numerical study of dendritic solidification of an ammonium chloride–water solution inside a vertical rectangular cavity is performed. Utilizing the volumetric averaging technique, one set of conservation equation is derived which is valid for the pure liquid and solid regions as well as for the dendritic mushy zone. This approach avoids the complications usually associated with the solution of problems involving multiple regions which are of an irregular (and changing) shape. A number of experiments are performed to visualize and quantify the phase-change and convection processes in the

cavity. The shadowgraph results reveal that the solidification process induces a variety of double-diffusive convection patterns in the liquid, including plumes and layering. These convection processes are found to considerably influence the local solidification rates as well as to cause remelting of parts of the mushy zone.

While it has been possible to qualitatively predict some of the phase-change and double-diffusive phenomena observed in the experiments, the numerical simulation shows considerable disagreement with the measurements. A discussion of the deficiencies in the model leading to these discrepancies is presented and the major areas where the present model needs to be improved are identified. In conclusion, it can be said that the physical phenomena identified in the present study are significant in many applications. Accurate modeling of the double-diffusive processes during solidification of binary mixtures is, for example, important for the prediction of macrosegregation in alloy castings. An improved version of the present model might be useful in contributing to an improved understanding of these very important phenomena.

Acknowledgements—The work reported in this paper was supported, in part, by the National Science Foundation under Grant No. CBT-8313573. Computer facilities were made available by Purdue University Computing Center.

NOMENCLATURE

A	aspect ratio, H/L
c	specific heat (J kg K^{-1})
C	mass fraction H_2O
d	diameter (m)
D	mass diffusivity (m^2 s^{-1})
g	gravitational acceleration (m s^{-2})
F	inertia coefficient
h	enthalpy (J kg^{-1})
Δh	latent heat of fusion (J kg^{-1})
H	height of enclosure (m)
k	thermal conductivity (W m K^{-1})
k^*	thermal conductivity ratio, $\bar{k}/k_l$
K	permeability (m^2)
L	length of enclosure (m)
Le	Lewis number, α_l/D_l
M_s	volumetric specific surface area (m^{-1})
p	dimensionless pressure, $PL^2/(\rho_l\alpha_l^2)$
P	pressure (N m^{-2})
Pr	Prandtl number, ν_l/α_l
Ra	Rayleigh number, $g\beta_l(T_H-T_C)L^3/(\nu_l\alpha_l)$
R_s	stability number, $\beta_c C_E/\beta_T(T_H-T_C)$
Ste	Stefan number, $c_l(T_H-T_C)/\Delta h$
t	time (s)
T	temperature (K)
u	dimensionless velocity, UL/α_l
U	velocity (m s^{-1})
x	horizontal coordinate (m)
y	vertical coordinate (m)

Greek symbols

α	thermal diffusivity, $k/\rho c$ (m^2 s^{-1})
β_c	concentration expansion coefficient
β_T	thermal expansion coefficient (K^{-1})
γ	dimensionless slope of liquidus line $\Gamma C_E/(T_H-T_C)$
Γ	slope of liquidus line (K)
ε	liquid volume fraction
η	dimensionless vertical coordinate, y/L
Θ	dimensionless temperature, $(T-T_C)/(T_H-T_C)$
κ	segregation coefficient, C_s/C_l
ν	kinematic viscosity (m^2 s^{-1})

ξ dimensionless horizontal coordinate, x/L
ρ density (kg m^{-3})
ρ^* density ratio, $\bar{\rho}/\rho_l$
$(\rho c)^*$ thermal capacitance ratio, $\overline{\rho c}/\rho_l c_l$
τ dimensionless time, $t\alpha_l/L^2$
Φ dimensionless concentration, C/C_E

Subscripts
C cold wall
eff effective value
E eutectic
H hot wall
in initial
l liquid
p pure
ref reference value
s solid

Superscripts
$\bar{}$ average value.

REFERENCES

1. H. E. Huppert and J. S. Turner, Double-diffusive convection. *J. Fluid Mech.* **106,** 299–329 (1981).
2. C. F. Chen and D. H. Johnson, Double-diffusive convection: a report on an Engineering Foundation Conference. *J. Fluid Mech.* **138,** 405–416 (1984).
3. G. S. Cole and G. F. Bolling, The importance of natural convection in castings. *Trans. Am. Instn Mech. Engrs* **233,** 1568–1572 (1965).
4. R. M. Sharp and A. Hellawall, The incidence of convection during solidification. *J. Crystal Growth* **12,** 261–262 (1972).
5. J. D. Verhoeven, K. K. Kingery and R. Hofer, The effect of solute convection upon macrosegregation in off-eutectic composite growth. *Metall. Trans.* **6B,** 647–652 (1975).
6. W. J. Boettinger, F. S. Biancaniello and S. R. Coriell, Solutal convection induced macrosegregation and the dendrite to composite transition in off-eutectic alloys. *Metall. Trans.* **12A,** 321–327 (1981).
7. J. D. Hunt and K. A. Jackson, Binary eutectic solidification. *Trans. Am. Instn Mech. Engrs* **236,** 843–852 (1966).
8. K. A. Jackson, J. D. Hunt, D. R. Uhlmann and T. P. Seward, On the origin of the equiaxed zone in castings. *Trans. Am. Instn Mech. Engrs* **236,** 149–158 (1966).
9. R. J. McDonald and J. D. Hunt, Fluid motion through the partially solid regions of a casting and its importance in understanding A-type segregation. *Trans. Am. Instn Mech. Engrs* **245,** 1993–1999 (1969).
10. R. J. McDonald and J. D. Hunt, Convective fluid motion within the interdendritic liquid of a casting. *Metall. Trans.* **1,** 1787–1788 (1970).
11. S. M. Copley, A. F. Giamei, S. M. Johnson and M. F. Hornbecker, The origin of freckles in unidirectionally solidified castings. *Metall. Trans.* **1,** 2193–2204 (1970).
12. S. Asai and I. Muchi, Theoretical analysis and model experiments on the formation mechanism of channel-type segregation. *Trans. Iron Steel Inst. Japan* **18,** 90–98 (1978).
13. J. Szekely and A. S. Jassal, An experimental and analytical study of the solidification of a binary dendritic system. *Metall. Trans.* **9B,** 389–398 (1978).
14. A. K. Sample and A. Hellawell, The mechanism of formation and prevention of channel segregation during alloy solidification. *Metall. Trans.* **15A,** 2163–2173 (1984).
15. C. F. Chen and J. S. Turner, Crystallization in a double-diffusive system. *J. geophys. Res.* **85,** 2573–2593 (1980).
16. J. S. Turner and L. B. Gustafson, Fluid motions and compositional gradients produced by crystallization or melting at vertical boundaries. *J. Volcan. Geoth. Res.* **11,** 93–125 (1981).
17. H. E. Huppert and R. S. J. Sparks, Double-diffusion convection due to crystallization in magmas. *Ann. Rev. Earth Planet. Sci.* **12,** 11–37 (1984).
18. R. Farhadieh and R. S. Tankin, A study of the freezing of sea water. *J. Fluid Mech.* **71,** 293–304 (1975).
19. B. W. Grange, R. Viskanta and W. H. Stevenson, Interferometric observation of thermohaline convection during freezing of saline solutions. *Letters Heat Mass Transfer* **4,** 85–92 (1977).
20. R. Mehrabian, M. Keane and M. C. Flemings, Interdendritic fluid flow and macrosegregation; influence of gravity. *Metall. Trans.* **1,** 1209–1220 (1970).
21. N. Streat and F. Weinberg, Macrosegregation during solidification resulting from density differences in the liquid. *Metall. Trans.* **5,** 2539–2548 (1974).

22. T. Fujii, D. R. Poirier and M. C. Flemings, Macrosegregation in a multi-component low alloy steel. *Metall. Trans.* **10B**, 331–339 (1979).
23. A. L. Maples and D. R. Poirier, Convection in the two-phase zone of solidifying alloys. *Metall. Trans.* **15B**, 163–172 (1984).
24. S. D. Ridder, S. Kou and R. Mehrabian, Effect of fluid flow on macrosegregation in axisymmetric ingots. *Metall. Trans.* **12B**, 435–447 (1981).
25. W. Stiller, Wärme- und Stofftransport bei der Erstarrung von Kokillenguss. Ph.D thesis, University of Hannover, Hannover, F.R.G. (1982).
26. W. G. Gray and K. O'Neill, On the general equations for flow in porous media and their reduction to Darcy's law. *Water Resources Res.* **12**, 148–154 (1976).
27. W. G. Gray, A derivation of the equations for multi-phase transport. *Chem. Engng Sci.* **30**, 229–233 (1975).
28. W. G. Gray, General conservation equations for multi-phase systems : 4. constitutive theory including phase change. *Adv. Water Resources* **6**, 130–140 (1983).
29. C. Beckermann, Melting and solidification in binary systems with double-diffusive convection in the melt. Ph.D thesis, Purdue University (1987).
30. G. S. Beavers and E. M. Sparrow, Non-Darcy flow through fibrous porous media. *J. Appl. Mech.* **36**, 711–714 (1969).
31. S. Patankar, *Numerical Heat Transfer and Fluid Flow*. Hemisphere, New York (1980).
32. C. Beckermann and R. Viskanta, Natural convection solid/liquid phase-change in porous media. *Int. J. Heat Mass Transfer* **36**, 35–46 (1988).
33. C. Beckermann, S. Ramadhyani and R. Viskanta, Natural convection flow and heat transfer between a fluid layer and a porous layer inside a rectangular enclosure. In *Natural Convection in Porous Media* (Edited by V. Prasad and N. A. Hussain), pp. 1–12. ASME, New York (1986).
34. *International Critical Tables of Numerical Data, Physics, Chemistry and Technology* **3**, 60 and **4**, 218 (1928).
35. S. A. Thorpe, P. K. Hutt and R. Soulsby, The effect of horizontal gradients on thermohaline convection. *J. Fluid Mech.* **38**, 375–400 (1969).